Heliyon 10 (2024) e28153

Contents lists available at ScienceDirect

Heliyon

journal homepage: www.cell.com/heliyon

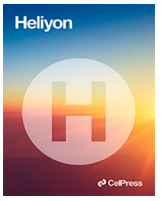

Research article

Synthesis, characterization and application of steel waste-based iron oxide nanoparticles for removal of heavy metals from industrial wastewaters

Tumutungire Mwebembezi [a], Joel Wakatuntu [a], Joseph Jjagwe [a], Christopher Kanyesigye [c], Robinah N. Kulabako [b], Peter Wilberforce Olupot [a,*]

[a] Department of Mechanical Engineering, College of Engineering, Design, Art and Technology, Makerere University, P.O. Box 7062, Kampala-Uganda
[b] Department of Civil and Environmental Engineering, College of Engineering, Design, Art and Technology, Makerere University, P.O. Box 7062, Kampala-Uganda
[c] National Water and Sewerage Corporation, Plot 3, Nakasero P.O BOX 7053 Kampala, Uganda

ARTICLE INFO

Keywords:
Steel pickling waste powder
Nanoparticle synthesis
Iron oxide nanoparticles
Heavy metals
Industrial wastewater treatment

ABSTRACT

Water treatment and reuse can avail more clean and safe water for human use. In this study, iron oxide waste powder generated from the steel pickling process was used to develop iron oxide nanoparticles (IONPs) using solution gelation synthesis process. The powder and developed IONPs were characterized by X-ray fluorescence and diffraction (XRF, XRD), scanning electron microscopy, Fourier-transform infrared spectroscopy, and Brunauer-Emmett-Teller (BET) analyses. Adsorption experiments were carried out on synthetic water with lead and chromium metal ions. The adsorption data were analysed with Langmuir and Freundlich models. Adsorption kinetics were also analysed with Pseudo-First-Order and Pseudo-Second-Order models using non-linear regression. The synthesized IONPs were porous with active surface functional groups of hydroxyl bonds, with BET specific surface area of 325.02 m^2/g. XRD results confirmed the cubic spinel structure of IONPs with particle sizes of 20–30 nm. The nanoparticles at a dosage of 0.35 g in 10 mL for 50 min effectively removed Pb(II) and Cr(VI) metal ions up to 99.9% from both synthetic water and industrial wastewater. The adsorption capacity (q_{max}) of IONPs was found to be 417 and 326.80 for Pb(II) and Cr(VI) respectively. Freundlich isotherm model data fitted best for the removal of both metal ions. The regression values for kinetic models confirmed that pseudo-second-order best fit the adsorption of both Pb(II) and Cr(VI) confirming chemisorption processes. This study contributes to elucidating alternative application of pickling waste from the steel rolling mills for the benefit of heavy metal removal in industrial wastewater.

1. Introduction

Lead and chromium are well-known heavy metals that pose significant threats to human health and the environment due to their toxicity and persistence in various industrial process waste streams [1]. Lead (Pb) is a highly toxic metal that can cause severe health effects, particularly in children, even at low exposure levels [2]. The maximum allowable concentration of Pb^{2+} in water effluents as set by international and most country-based bodies is 10 μg/L. Nevertheless, a stricter limit of 5 μg/L is proposed by World Health

* Corresponding author.
E-mail address: peter.olupot@mak.ac.ug (P.W. Olupot).

https://doi.org/10.1016/j.heliyon.2024.e28153
Received 19 September 2023; Received in revised form 27 February 2024; Accepted 13 March 2024
Available online 15 March 2024

Organization [3]. Ecosystems near point sources of lead exhibit a wide range of adverse effects including losses in biodiversity, changes in community composition, decreased growth and reproductive rates in plants and animals, and neurological effects in vertebrates [4]. Chromium (Cr) exists in several oxidation states, with hexavalent chromium (Cr(VI)) being the most toxic and carcinogenic form. It is commonly found in industrial effluents and is associated with serious health risks, including respiratory and gastrointestinal disorders, as well as liver and kidney damage [5].

Efforts to mitigate the harmful effects of lead and chromium contamination have been ongoing for many years. Various approaches have been employed to remove these heavy metals from contaminated water and wastewater, including precipitation, coagulation-flocculation, ion exchange, reverse osmosis, and activated carbon adsorption [6]. While these methods have shown varying degrees of effectiveness, they often suffer from certain drawbacks. Precipitation and coagulation-flocculation techniques generate large volumes of sludge, which require further treatment and disposal [7]. Ion exchange and reverse osmosis are energy-intensive processes and may not be economically viable for large-scale applications [8]. Activated carbon adsorption, although widely used, can be expensive and requires frequent regeneration or replacement [9].

In recent years, the emergence of nano-adsorbents as promising materials for heavy metal removal has garnered significant attention [10]. Nano-adsorbents offer unique properties, such as large specific surface area, high reactivity, and tuneable surface chemistry, which make them highly efficient in adsorbing heavy metal ions from aqueous solutions [11]. Among the various types of nano-adsorbents, iron oxide nanoparticles (IONPs) have shown great potential due to their excellent adsorption capacities and ease of synthesis [12]. IONPs offer a high surface area, regenerability, rapid removal rate, selective binding, scalability, and compatibility which makes them advantageous for heavy metal removal [13]. Several studies have explored the use of IONPs for the removal of lead and chromium from contaminated water sources. For instance, Mahanty et al. [14] demonstrated the successful application of IONPs in removing lead ions from industrial wastewater, achieving a removal efficiency of over 90%. Similarly, Chatterjee et al. [15] investigated the adsorption behaviour of chromium on IONPs and reported a reduction in Cr(VI) concentration of up to >99%, highlighting the effectiveness of IONPs in chromium removal.

The synthesis of IONPs can be achieved through various approaches, including chemical precipitation, sol-gel methods, hydrothermal synthesis, and thermal decomposition. These methods offer control over the size, morphology, and surface properties of the nanoparticles, allowing optimization for specific adsorption applications [16]. However, the production of IONPs using conventional approaches often involves the use of expensive chemical precursors, high-energy requirements, and complex synthesis procedures, which can limit their scalability and practicality [17].

To address the limitations of conventional approaches, alternative methods for IONP synthesis have gained attention, particularly those utilizing steel waste materials. Steel waste materials, such as steel slag or steel industry by-products, present a cost-effective and sustainable source of iron for IONP synthesis. These waste materials contain high amounts of iron oxide, which can be extracted and used as a precursor for generation of IONPs [18]. By repurposing steel waste materials, the production of IONPs becomes economically viable, environmentally friendly, and contributes to the circular economy. Amongst the common steel waste-based materials is iron oxide powder, which is generated from steel pickling processes in steel companies. This waste powder is generated in large quantities and thus require a large storage area. For example, Roofings Rolling Mills, a major steel processing company in Uganda, alone generates about 800 metric tons of iron oxide waste annually [19]. This oxide is usually stockpiled and/or landfilled as a solid waste, and due to its high acidity content, it poses a threat to the environment [20]. Additionally, the oxide has a potential to leach heavy metals, such as lead or chromium, from other waste materials present in the landfills. Given the nature of this oxide waste (over 70% purity in form of α-Fe2O3), it can be used as a precursor to generate IONPs for removal of pollutants from water [18]. However, studies that have utilized steel waste materials for generation of IONPs for remediation of heavy metal ions have mainly focused on mill scale [21–23], steel pickling liquor [24–26], iron sludge [27], and direct iron reduction sludge [28]. There is a dearth of studies on the utilization of iron oxide waste powder for synthesis of IONPs suitable for adsorption of heavy metals. The novelty of this work lies in demonstrating the suitability of iron oxide powder generated from steel pickling process for synthesis of IONPs. This work also reveals the adsorption capacity for selected heavy metals by the generated IONPs. The attributes of iron oxide waste-derived iron oxide nanoparticles make them attractive for use in various fields, including biomedicine, environmental remediation, catalysis, and energy storage. The high abundance of iron oxide waste powder, cost effectiveness, reduced chemical usage, biocompatibility, magnetic properties, control over nanoparticle properties and scalability contribute to their advantages over conventional sources in the production of IONPs.

2. Materials and methods

2.1. Material collection and preparation

Iron oxide waste powder (IOWP) was sourced from Roofings Rolling Mills Limited, Namanve Industrial Area, Mukono District (0° 20′ 27″N, 32° 41′ 56″E) which is the largest steel milling company in Uganda. The IOWP was then stored in a clean polythene bag to avoid contamination from the environment. Hydrochloric acid (35% extra pure), Ammonia hydroxide solution (30% extra pure, specific gravity 0.89) and ferrous chloride (Hydrated 98% extra pure) used were of analytical grade and were used as received without any further purification and were obtained from Perkins Laboratory, Kampala, Uganda.

2.2. Synthesis of iron oxide nanoparticles

A solution gelation procedure similar to the one derived by Matijevic and Scheiner [29] was used to produce iron oxide

nanoparticles from the powders. All glassware used in the synthesis was washed with 2% nitric acid followed by rinsing with double distilled water to remove any traces of organic or inorganic contamination before being used in experimentation. Ammonia solution was prepared in varying concentrations of 2.5, 5, 10, and 15% to be used as a precipitate. Hydrochloric acid of 8 M concentration was prepared in quantities of 100 mL. Ten (10) grams of IOWP were dissolved in 100 mL HCl acid. The resultant solution was heated at 80 °C for 2 h under constant agitation at 250 rpm. 5g of ferrous chloride were dissolved in 100 mL of deionized water. The IOWP-HCl solution was then mixed with the ferrous chloride solution, and thoroughly stirred for 1 h at room temperature to make 200 mL of final solution. Ammonia Solution of different concentrations was added to the 200 mL solution dropwise under magnetic stirring at 250 rpm until a black slurry was formed. The resulting slurry was continuously washed with deionized water until a neutral pH of 7 was reached. The resulting black slurry were the iron oxide nanoparticles. Thereafter, the iron oxide nanoparticles (IONPs) were filtered out using a Whatman 41 filter paper, dried at 90 °C for 2 h in an oven, and later calcined at 300 °C for 2 h. The IONPs were later stored in a moisture-free environment.

2.3. Characterization of the iron oxide waste powder and iron oxide nanoparticles

2.3.1. Chemical composition and Particle size distribution

X-ray fluorescence (XRF) was used to determine the chemical composition of the IOWP. This was done using test methods: US EAS 148–2:2017. Particle size distribution was done to determine the size and range of particles present in the IOWP using the sieve analysis method. A Zetasizer was used to analyze the average particle size of the iron oxide nanoparticles. The hydrodynamic diameter of aqueous suspensions of iron oxide nanoparticles was measured by Multi-Angle Dynamic Light Scattering (MADLS) with a Malvern Zetasizer Ultra Blue Instrument using a laser (He–Ne) wavelength of 633 nm and a scattering angle of 173°. The temperature measurement was fixed at 25 °C. The viscosity and the refractive index of water were set to 0.8872 cp and 1.33, respectively. For IONPs, the refractive index was set to 2.008. The hydrodynamic diameter was calculated from the average of three measurements.

2.3.2. Morphology

Scanning electron microscopy (SEM) with a SEM Zeiss sigma 300 was used to analyze the morphology of IOWP and IONPs. The sample was adhesively bonded to the sample stub using carbon tape and then coated with a 2 nm layer of chromium. The sample stub containing the sample was inserted in the SEM sample compartment to start the capturing of the SEM images at a 10 kV acceleration voltage.

2.3.3. Fourier transform infrared (FTIR) spectroscopy

FTIR was used to study the surface interaction of the IOWP and the synthesized IONPs with other molecules involved in the synthesis and stabilization of the nanoparticles. The FT-IR spectra were collected with a spectrometer in the range of 4000–400 cm^{-1}. The Compact FT-IR Spectrometer (Alpha II) was used. Origin Software 2019b was used to plot graphs.

2.3.4. Surface area and mean pore diameter determination

The BET surface area and mean pore diameter of the IOWP and iron oxide nanoparticles samples were determined from nitrogen adsorption-desorption isotherm using the Brunauer-Emmett-Teller (BET) method. Before measuring nitrogen gas adsorption, the samples were vacuum degassed for at least 2 h to remove any adsorbed species in the sample pores. Adsorption-desorption of the samples was thereafter done by N_2 adsorption at 77 K.

2.3.5. X-ray diffraction

X-ray diffraction was used to extract structural information of the crystal lattice of the nanoparticles. The material was irradiated with incident X-rays and then the intensities and scattering angles of the X-rays that leave the material were measured. The intensity of the scattered X-rays was plotted as a function of the scattering angle. The structure of the material was determined from the analysis of the location in angle, and the intensities of scattered intensity peaks with help of X'pert Software.

2.4. Water treatment

2.4.1. Wastewater Collection

The wastewater sample was obtained from Global Paints Factory, Uganda whose effluent is highly expected to be contaminated with heavy metals. Samples were picked on three different sampling occasions at intervals of one week. The collected samples were stored in a cool box at approximately 4 °C to prevent any biological activity that could affect the analysis results. The samples were then characterized from the Government Analytical Laboratory in Wandegeya, Kampala-Uganda and the Public Health and Environmental Engineering Laboratory, Department of Civil and Environmental Engineering, Makerere University. The effluent was characterized for copper, lead, chromium, and zinc contamination levels using the Agilent 200 series AA Atomic absorption spectrometer with hollow cathode lamps at respective wavelengths as radiation sources. Additionally, other characteristics of effluent such as Total Organic Carbon, pH, Total Alkalinity, turbidity, apparent color, and Electrical conductivity were determined to find out their compliance with effluent discharge standards. The Palintest Photometer Bluetooth 7500 was used to measure total alkalinity and a Hach DR/890 colorimeter was used to measure turbidity and apparent color. Hach HQ30d rugged multi-meter was used to measure electrical conductivity.

2.4.2. Preparation of synthetic wastewater

Synthetic wastewater samples were prepared by mixing standard heavy metal solutions of Lead nitrate $Pb(NO_3).4H_2O$ and Chromium salt solutions. Stock solutions of these heavy metal solutions were prepared in concentrations of 1 ppm and 0.5 ppm. The chosen ranges of concentration of heavy metal ions reflect typical levels of lead and chromium ions found in the environmental samples used in this study. By selecting concentrations within the observed range, this helped mimic real-world conditions and create synthetic wastewater that closely resembled the environmental conditions under study.

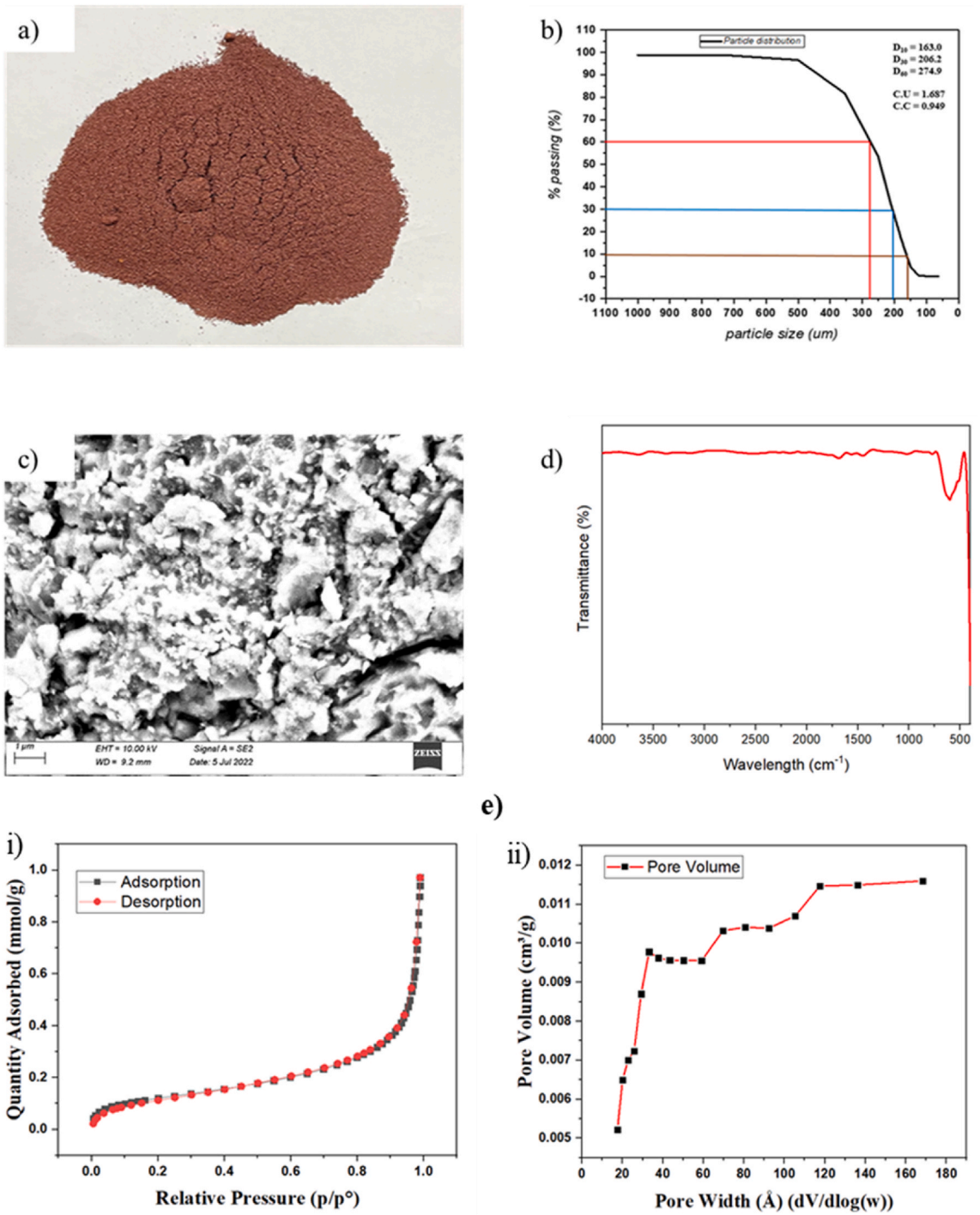

Fig. 1. IOWP (a), Particle size distribution of IOWP (b), Scanning electron micrograph of IOWP (c), FT-IR Spectra for IOWP (d), IOWP N_2 Desorption/Adsorption Isothermals at 77 K (e) (i) and pore size distribution (e) (ii).

2.4.3. Adsorption experiments procedure

Batch experiments were conducted to investigate the influence of contact time and initial concentration on metal ions by the iron oxide nanoparticles. An aqueous solution of synthetic wastewater containing Lead (1 ppm) and Chromium (0.5 ppm) metal ions was used to determine the best treatment conditions from the batch experiments. The best conditions, including time and dosage of the nanoparticles that successfully removed the heavy metals in the synthetic wastewater, were then applied to the environmental wastewater sample obtained from Global Paints Factory. To minimize changes in all other variables except the one being tested, control experiments were also performed alongside the batch experiments. The control experiment was the wastewater without iron oxide nanoparticles. Adsorbent dosages of 0.1 g and 0.35 g were chosen based on previous studies [30]. By choosing these different dosages, a dosage that achieves the maximum adsorption capacity or efficiency was identified. To observe the equilibrium behaviour of the adsorption process, the lower dosage of 0.1 g was used to assess the adsorption capacity at the early stages of the process, where the adsorbent is not yet saturated. Higher dosage of 0.35 g was chosen to investigate at near saturation.

Centrifuge tubes containing 0.1g, 0.35 g of adsorbent, and 10 mL of synthetic water at pH 7.1 were placed on an orbital shaker at room temperature (25 °C). The speed of the orbital shaker was set to 250 rpm. At intervals of 5, 10, 20, 30, 40, 50 min, and 1, 5, 10, 24, and 30 h, the magnetic adsorbent was separated from the solutions using a permanent magnet. This was done for all the different concentrations of synthetic wastewater for both lead and chromium. The initial and final metal ions concentrations were determined using the Agilent 200 series AA Atomic absorption spectrometer with hollow cathode lamps at respective wavelengths as radiation sources. An air acetylene flame was used for determination of lead and chromium ions. Calibration curves for both metals were constructed, and their respective absorbance values were obtained in graphical form as concentration versus absorbance.

The removal efficiency of metal ions adsorbed onto the magnetic adsorbent was calculated according to Equation (1):

$$\text{Removal efficiency } (\%) = \left(\frac{Co - Ct}{Co}\right) \times 100 \quad (1)$$

Where C_o and C_t (mg/L) are initial concentrations and the concentration of heavy metal ions at any time t, respectively.

3. Results and discussion

3.1. Physicochemical properties of iron oxide waste powder

3.1.1. Chemical composition

The IOWP was a red-brown powder (Fig. 1(a)) and was insoluble in water. XRF analysis revealed that iron (III) oxide was the major compound contributing 97.23% of the total mass of the waste as indicated in Table 1. The high percentage of iron (III) oxide indicates the presence of minimal impurities in the red oxide. The red oxide, therefore, did not require any further purification.

3.1.2. Particle size distribution

Using the sieve analysis method, the particle size distribution of as received-iron oxide waste powder is shown in Table 2 and Fig. 1 (b).

After grading, the particle size D10 was obtained as 163.0 μm whereas D60 was 274.9 μm (Figs. 4–2). D10, D30 and D60 represent the particle size below which 10%, 30% and 60% of the particles in the sample are smaller respectively. 30%, of IOWP was finer than 206.2 μm size (D30). The coefficient of uniformity, computed as the ratio of D60 to D10 was 1.687 which implied a uniform mix of particles [31]. The coefficient of curvature computed by comparing the particle diameters at specific percentiles, namely D10, D30, and D60, to assess the skewness of the particle size distribution was determined as 0.949. This implied that the IOWP particle sizes did not have much variation. A properly controlled and homogeneous particle size distribution is important in the synthesis of nanoparticles for adsorption purposes. This is because the nanoparticles' size and size distribution directly affect their surface area and pore structure, which are essential for adsorption [32]. A narrow size distribution of the IOWP with a high coefficient of uniformity ensures that the synthesized nanoparticles have similar size and shape, which leads to a more uniform pore structure and a higher adsorption capacity. Also, a lower coefficient of curvature (less than 4) suggests a more uniform distribution which minimizes the occurrence of bigger particle sizes in the synthesized nanoparticles that could limit the adsorption capacity [33].

3.1.3. SEM analysis

Fig. 1(c) shows the SEM imaging of the IOWP. The analysis reveals that the IOWP surface exhibited a heterogeneous structure with minimal crevices and varying particle sizes and shapes.

3.1.4. FTIR analysis

The FTIR analysis was done on the IOWP to identify the functional groups. Fig. 1(d) shows the bands of the FTIR spectra that were

Table 1
Chemical composition of the iron oxide waste picked from Roofings Steel Mill.

Iron Oxide	Compound metal oxide (m/m%)					
	Fe_2O_3	LOI (Loss on Ignition)	SiO_2	Al_2O_3	CaO	MgO
	97.23	1.89	0.27	0.11	0.25	0.25

Table 2
Quantities retained on the different sieves.

Particle size distribution (Sieve analysis)											
Sieve aperture (μm)	1000	710	500	355	250	212	180	150	125	90	63
Qty retained (g)	1.2	0.2	1.9	14.3	27.3	19.7	14.8	12.5	3.8	0.4	0

obtained for the IOWP. The spectrum indicated one typical intense peak at 540 cm^{-1}. This is in agreement with other studies [34–37] which have indicated only a single intense peak for pure hematite usually observed between 463 and 555 cm^{-1}. This band is assigned to the Fe–O stretching/vibrational band in octahedral sites of hematite [35]. This, therefore confirms that IOWP is Hematite. Nonetheless, there were small peaks attained between 1650 and 1500 cm^{-1} (Fig. 1(d)), and these could be ascribed to O–H stretching band [38] resulting from residual moisture present on the surface of IOWP during sample analysis.

3.1.5. Brunauer-Emmett-Teller (BET) analysis

The BET analysis was done to determine the surface area of IOWP to get information about their adsorption and dissolution properties. The specific surface area of the IOWP was established as 9.7265 m^2/g. Fig. 1 (e) (i) shows the N_2 adsorption-desorption isotherms, and Fig. 1(e)(ii) shows the pore size distribution diagrams of the IOWP. Based on IUPAC isotherms classification, Fig. 1 (e) (i) shows that the N_2 adsorption-desorption isotherm of IOWP is of type III having H_3 type hysteresis loop. This shape shows that the adsorbent-adsorbate interaction is weak indicating that the product has a typical macroporous structure. This can be further evidenced by Fig. 1 (e) (ii), in which the pore size distribution does not have a uniform peak, and keeps on increasing confirming a macroporous structure that is directly related to a low surface area. Table 3 is a summary of the parameters calculated from nitrogen adsorption-desorption isotherm for IOWP.

3.2. Physicochemical properties of the iron oxide nanoparticles

3.2.1. FTIR analysis of the synthesized iron oxide nanoparticles

The FTIR analysis was done on the synthesized iron oxide nanoparticles to identify the functional groups. All the samples show bands near 3400 cm^{-1} and 1630 cm^{-1} attributed to O–H stretching and bending, respectively due to physiosorbed water molecules (Fig. 2(a)). All samples show characteristic peaks at around 580 cm^{-1} - 600 cm^{-1}, corresponding to the Fe–O stretching vibration mode and hydroxyl bonds. The presence of hydroxyl groups is an indication of the sample's exposure to moisture. The origination of two sharp absorption bands at 468 cm^{-1} and 554 cm^{-1} is due to formation of Fe–O bonds which confirms the formation of iron oxide crystals [39]. The bands at 425 cm^{-1}, and 557 cm^{-1} indicate Fe–O bonds of magnetic nanoparticles similar to the study by Basavegowda et al. [40]. The change in the intensity of the peaks at around 3020 cm^{-1}, 2340 cm^{-1} and 1620 cm^{-1} in the graphs is attributed to different concentrations of ammonium solution. The intensity of the peaks increases with increasing concentration of ammonia solution which indicates a higher degree of reduction. A study by Maleki et al. [41] concluded that iron oxide nanoparticles with smaller sizes or different crystal structures are formed when the concentration of the reducing agent is high (above 30%), which might have an impact on the FTIR spectra.

3.2.2. BET surface area

The BET surface area of the adsorbent material is the surface area of the adsorbent's unit mass. Since adsorption is a surface reaction, a high surface area is often regarded as an important property to enhance the adsorption capacity. The adsorption of the adsorbate increases as the adsorbent's surface area increases due to generation of a large number of adsorbing sites. The nitrogen adsorption-desorption isotherms of the synthesized nanoparticles are shown in Fig. 2(b). The obtained graph for (i) and (ii) synthesized with 2.5% and 5% molar ammonium solution respectively showed the type IV isotherms with type H_3 hysteresis loops according to The Brunauer-Deming-Deming-Teller (BDDT) classification, indicating the presence of mesopores (2–50 nm). The insets in Fig. 2(b) show the corresponding pore size distributions of the nanoparticles. The pore size distribution shows a high concentration of small pores with a narrow neck. This also indicates that adsorption occurs mainly in the neck of the pore and is slow to desorb because small pores with narrow necks have a lower rate of diffusion [42]. In a study by Zhang et al. [43], a type H_3 hysteresis loop according to BDDT classification indicates the presence of mesopores (2–50 nm) with a cylindrical pore mode, as seen in Fig. 2(b) (i) and (ii). The obtained graph for (iii) and (iv) synthesized with 10% and 15% molar solution respectively did not show any type of isotherm according to BDDT classification. This can be attributed to complex morphology or surface structure of the nanoparticles that is not well described

Table 3
Parameters calculated from nitrogen adsorption-desorption isotherm for IOWP.

Parameters	IOWP
BET surface area	9.7265 m^2/g
BJH desorption cumulative surface area of pores between 1.7 and 300 nm diameter	8.3133 m^2/g
Single point total pore volume of pores less than 130.9985 nm and diameter at p/p_o 0.98	0.0283 cm^3/g
BJH desorption cumulative pore volume of pores between 1.7 and 300 nm diameter	0.0103 cm^3/g
Average pore diameter (4V/A by BET)	11.6366 nm
BJH desorption average pore diameter (4V/A)	4.9578 nm

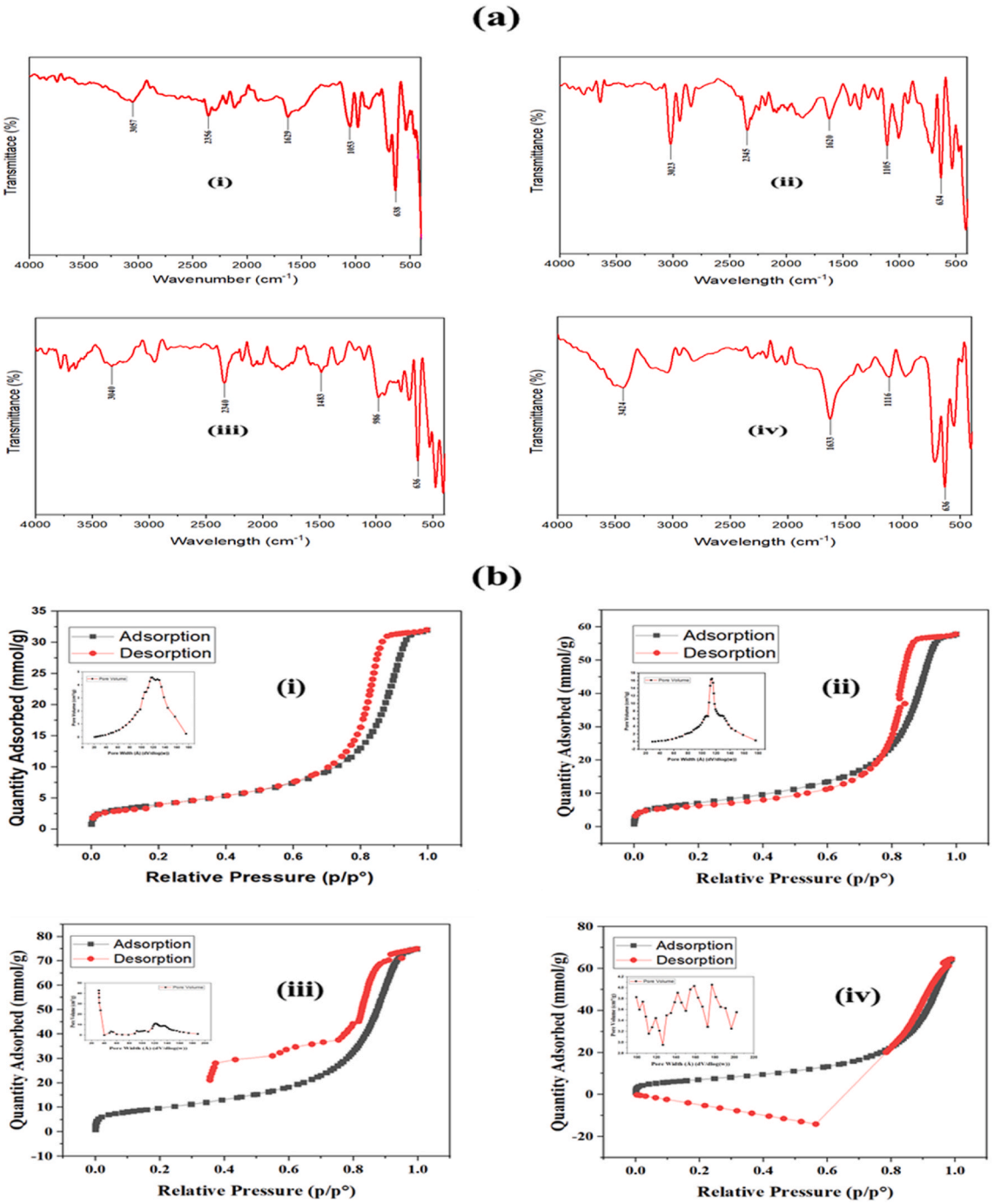

Fig. 2. (a) FT-IR Spectra of Iron oxide nanoparticles prepared using; 2.5% (i), 5% (ii), 10% (iii), and 15% (iv) ammonia solutions, (b) N_2 Desorption/Adsorption Isothermals at 77 K for Iron oxide nanoparticles prepared using ammonia solutions of; (i) 2.5%, (ii) 5%, (iii) 10%, and (iv) 15%.

by the standard isotherm models. The surface of iron oxide nanoparticles may include facets, edges, or other characteristics that might change adsorption energies or site densities and, as a result, alter the behavior of the gas sorption process as a whole [44].

The BET surface area, pore volume, and average diameter as obtained from the nitrogen adsorption-desorption are presented in Table 4. As the concentration of ammonium solution increased, the surface area was noted to decrease. This is because ammonium ions react with the iron oxide nanoparticles' surface during the reduction process using ammonia solution, which results in the removal of some of the iron oxide atoms from the surface in a process known as etching. Hence, more etching takes place and the surface area of

the iron oxide nanoparticles decreases with increasing ammonium solution reducing agent concentration [45].

From the results obtained, it was observed that the iron oxide nanoparticles prepared using a 2.5% concentration of ammonium exhibited better characteristics as compared to other nanoparticles prepared using other ammonium concentrations because of its greater surface area. For adsorption purposes, a larger surface area increases the number of adsorbing sites which increases efficiency. In a similar study done by Khanna et al. [46] to remove lead ions in water, a surface area of 171 m^2/g was reported and was able to remove up to 99% of lead ions.

3.2.3. SEM analysis of the synthesized iron oxide nanoparticles

Fig. 3(a) shows the SEM images of the synthesized iron oxide nanoparticles. The images reveal that some particles are agglomerated. Agglomerated iron oxide nanoparticles are often observed in the powders obtained by co-precipitation. Additionally, Fig. 3(a) reveals that the surface of the iron oxide nanoparticles exhibited a heterogeneous structure with numerous pores of various sizes and shapes. Iron oxide nanoparticles with a heterogeneous structure and numerous pores of various sizes as well as shapes have shown to be effective in removing contaminants from wastewater [47]. The heterogeneous structure of the IONPs enables the removal of numerous types of pollutants through a variety of methods, including physical adsorption, chemical adsorption, and electrostatic interactions. The pores in the IONPs give a large surface area for the adsorption of pollutants. The presence of different pore sizes and shapes in IONPs allows for the removal of contaminants of different sizes and shapes [12]. The removal of bigger pollutants, such as bacteria and viruses, may be facilitated by larger pores, whereas the removal of smaller molecules, such as organic compounds, may be facilitated by smaller pores.

3.2.4. XRD analysis of the synthesized nanoparticles

The XRD data of iron oxide nanoparticles presented in Fig. 3(b) agrees with the standard value of Fe_3O_4 (JCPDS file no: 65–3107). XRD analysis of the particles (Fig. 3(b)) shows well defined Bragg reflection characteristics of Fe_3O_4. The data shows intense diffraction peaks at $2\theta = 42.51^\circ$ (400) and minor peaks at 36.17° (311), 39.55° (222), 51.66° (422), 64.41° (440), 68.51° (531) and 75.45° (533) which confirms the cubic spinel structure of Fe_3O_4 nanoparticles. The absence of peaks at (104) and (110) plane orientations of the hematite form of Fe_2O_3 nanoparticles further confirms the pure crystalline magnetite form of the synthesized Fe_3O_4 nanoparticles [48]. The crystalline iron oxide nanoparticles have higher adsorption capacities for heavy metals than amorphous iron oxide nanoparticles. This is because the crystalline structure provides a larger surface area for adsorption and also promotes better interaction between the nanoparticles and the contaminants [43].

3.2.5. Particle size distribution

The hydrodynamic diameter sizes of the synthesized iron oxide were measured using a Zetasizer. The average particle sizes were found to be between 20 nm and 30 nm (Fig. 3(c)). This confirmed that the particles prepared were on a nano-scale. According to Morillo et al. [49], to increase the adsorption capacities, the size of the nanoparticles should be < 100 nm. The size of the nanoparticles is a significant factor when applied to water treatment.

3.3. Evaluation of the efficacy of developed iron oxide nanoparticles in wastewater treatment

3.3.1. Wastewater analysis

The quality characteristics of the wastewater samples are shown in Table 5 for the different sampling intervals. Also included in the table are the US EPA regulatory limits [50] and Uganda national effluent discharge standards [51] for the specified measured parameters.

From Table 5, the concentrations of lead and chromium in the wastewater were above the maximum permissible limit according to US EPA regulatory limits and Uganda national effluent discharge standards. This means that the concentrations of lead and chromium metals in the effluent are a great danger to the environment. Other parameters including TOC, turbidity, pH, total alkalinity, apparent color, and EC were within the permissible limits according to US EPA regulatory limits and Uganda National Standards (Table 5).

3.3.2. Influence of contact time and dosage of iron oxide nanoparticles

3.3.2.1. Lead. The results of adsorption studies conducted as a function of contact time involving Pb at a known concentration of 1 ppm and 0.5 ppm using an adsorbent dosage of 0.1 g and 0.35 g are presented in Fig. 4(a). The graphs suggest that the removal of Pb ions by the different dosages of the adsorbent occurred in two distinct steps: a relatively rapid phase (first 200 min), followed by an

Table 4
Surface area and their average diameter calculated from nitrogen adsorption-desorption isotherm for graphs A, B, C and D prepared using different molar ammonium solutions.

Parameters	Iron Oxide Nanoparticles			
	A	B	C	D
BET surface area	325.0212 m^2/g	284.8498 m^2/g	235.0494 m^2/g	233.1666 m^2/g
Average pore diameter (4V/A by BET)	13.0736 nm	13.0012 nm	13.5640 nm	15.2310 nm

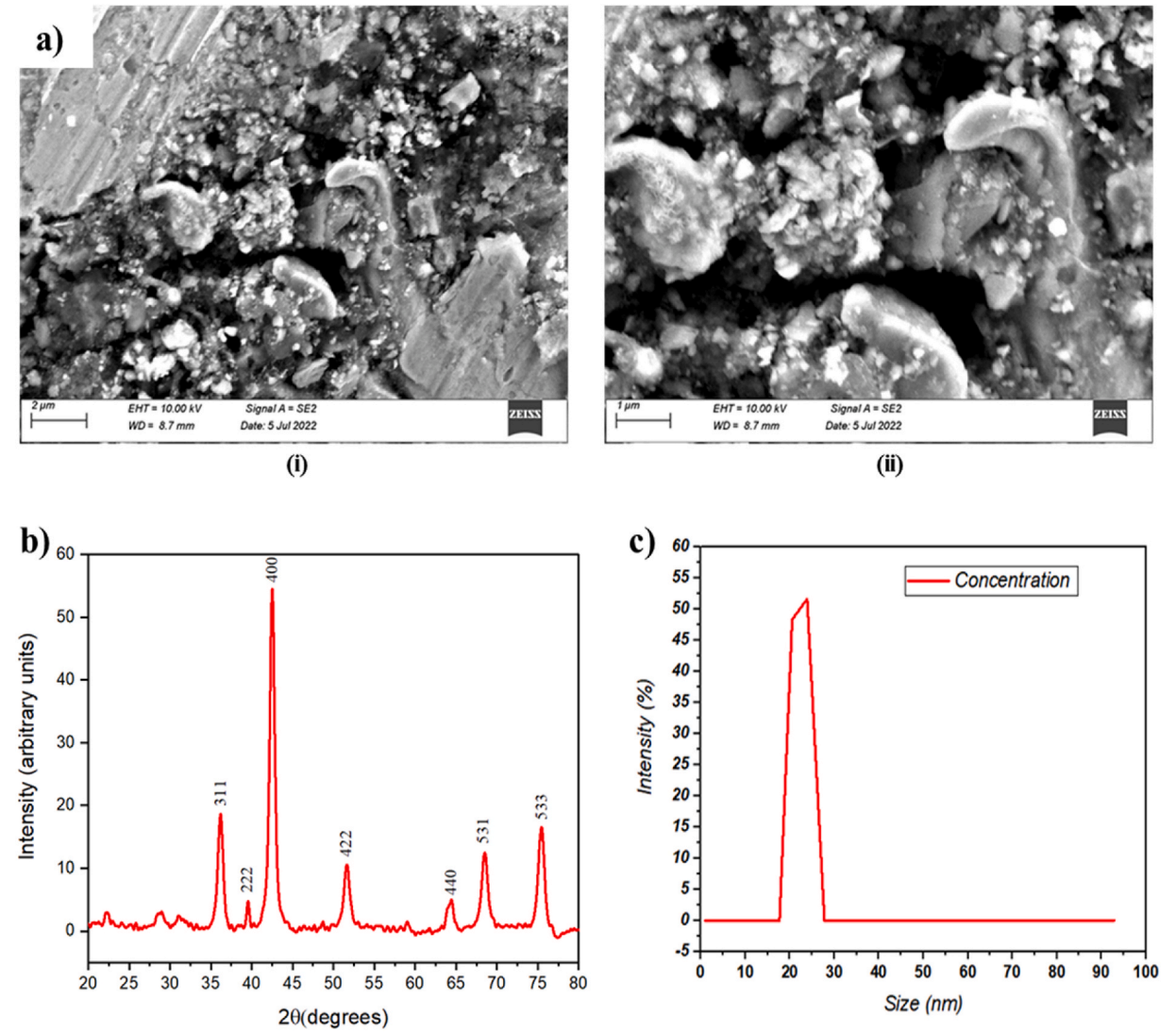

Fig. 3. (a) Scanning electron micrograph of Iron oxide nanoparticles at 2 µm (i) and 1 µm (ii), (b) XRD graph of the IONPs, (c) Particle size distribution of IONPs.

Table 5
Characteristics of the effluent water from Global Paints Factory.

Parameter	Sampling times					Permissible limits	
	1	2	3	Mean	S. D	US EPA	NEMA
Pb (mg/L)	0.3	0.42	0.235	0.32	0.094	0.015	0.1
Cr (mg/L)	1.14	0.64	0.125	0.64	0.508	0.1	0.05
TOC (mg/L)	19.9	19.9	19	19.6	0.520	75	50
Turbidity (FAU)	13	15	16	14.67	1.528	50	300
pH	7.1	7.6	7.6	7.43	0.289	6.5–8	5.0–8.5
Total Alkalinity (mg/L)	185	185	145	171.67	23.094	75–200	20–200
Apparent Color (PtCo)	82	99	65	82	17	400	300
EC (µs/cm)	947	982	906	945	31.059	50–1500	1000

increase until the equilibrium was reached. The necessary time to reach the equilibrium was about 300 min. A rapid phase removal was achieved for both concentrations of Pb ions with a dosage of 0.35 g. This is attributed to an increase in surface area where the adsorption takes place.

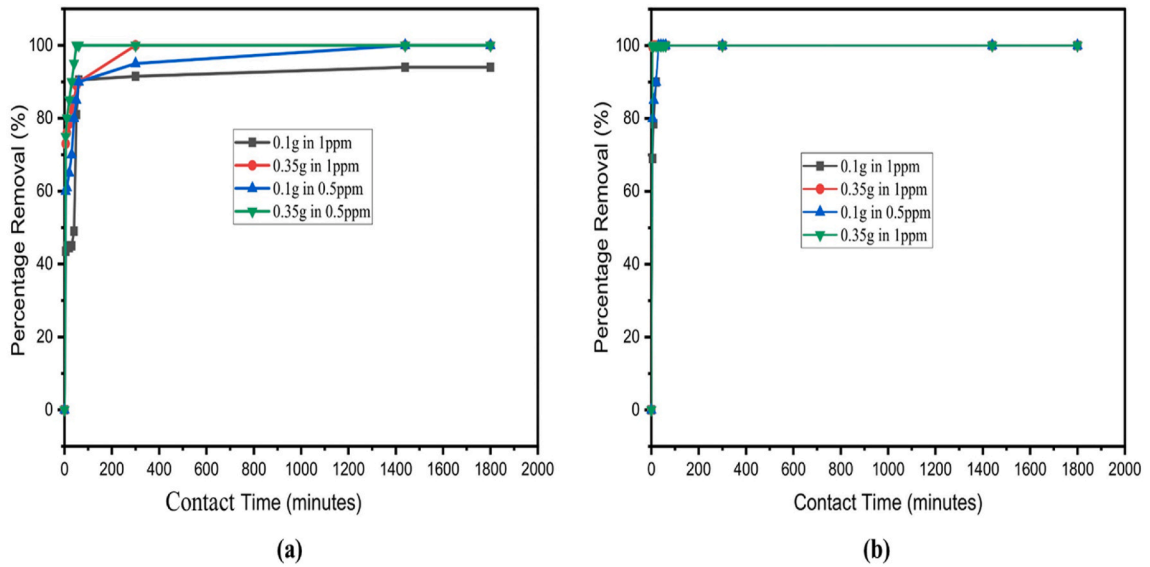

Fig. 4. Percent removal (%) of; (a) Lead metal versus contact time. 10 mL of aqueous solution (1 ppm and 0.5 ppm) were treated with 0.1g and 0.35g of nanoparticle, (b) Chromium metal versus contact time. 10 mL of aqueous solution (1 ppm and 0.5 ppm) were treated with 0.1 g and 0.35 g of nanoparticle.

3.3.2.2. Chromium. The results of adsorption studies conducted as a function of contact time involving Cr at a known concentration of 1 ppm and 0.5 ppm using an adsorbent dosage of 0.1 g and 0.35 g are presented in Fig. 4(b). The two graphs suggested that the removal of Cr ions by the different dosages of the adsorbent occurred at a relatively fast rate (first 50 min). The necessary time to reach the equilibrium was about 50 min. A rapid phase removal was also achieved for both concentrations of Cr ions with a dosage of 0.35 g. This is also attributed to an increase in surface area where the adsorption takes place. Compared with the previous studies on lead and chromium heavy metal adsorption done by Bagbi et al. [52], iron oxide nanoparticles in general show superior Pb and Cr adsorption capacities. Nanoparticle dosages of 0.35 g showed a higher adsorption capacity at both high and low concentrations of heavy metals.

3.3.3. Adsorption isotherms

3.3.3.1. Langmuir isotherm. The Langmuir isotherm model assumes the formation of a monolayer of metal molecules on the outer surface of the adsorbent after which no further adsorption takes place on the adsorbent surface. It explains the equilibrium distribution of metal ions between liquid and solid phases. With the help of Origin Software 2019, linear graphs were constructed as 1/qe versus 1/Ce.

Q_{max} value was calculated from the formula $q = \frac{Q_{max}.b.c}{1+b.c}$. This is the least sorption capacity of the adsorbent (on peak time interval) at equilibrium after which desorption starts.

The plots of 1/qe versus 1/Ce show that the adsorption of Pb^{2+} and Cr^{6+} gives a straight line which is represented in Fig. 5 (a). Values of q_m and b of the linear equation of Langmuir adsorption isotherm were derived from the slopes and intercepts of the linear plots of $1/qe$ versus $1/ce$ in Fig. 5(a). These values are represented in Table 6. The isotherm was found to be linear in most of the concentration ranges studies displaying with best linear correlation value $R^2 = 0.9997$ for lead when adsorbed to Iron Oxide Nanoparticles (IONPs). Whereas the correlation value was $R^2 = 0.9713$ for chromium adsorption to IONPs. Thus, confirming the monolayer coverage of lead and chromium (pollutants) on the applied sorbents. This means that adsorbates are in contact with the surface layer of the adsorbent.

3.3.3.2. Freundlich isotherm. The Freundlich isotherm suggests adsorption phenomena occur on heterogeneous surfaces. The empirical Freundlich isotherm equation, which is based on adsorption on heterogeneous sites, can be derived by supposing a logarithmic decrease in the enthalpy of adsorption with the increase in the number of adsorption sites, despite the Langmuir isotherm's assertion that enthalpy of adsorption does not depend on the concentration of metal ions adsorbed.

The mathematical form of the Freundlich equation is given in equation (2) and 3 [53]:

Linearized form:

$$q_e = K_f C_e^{1/n} \quad (2)$$

$$\log q_e = \log K_f + 1/n \log C_e \quad (3)$$

where K_f *is* adsorption capacity (L/mg), and $1/n$ is adsorption intensity and are both Freundlich constants. These are calculated from

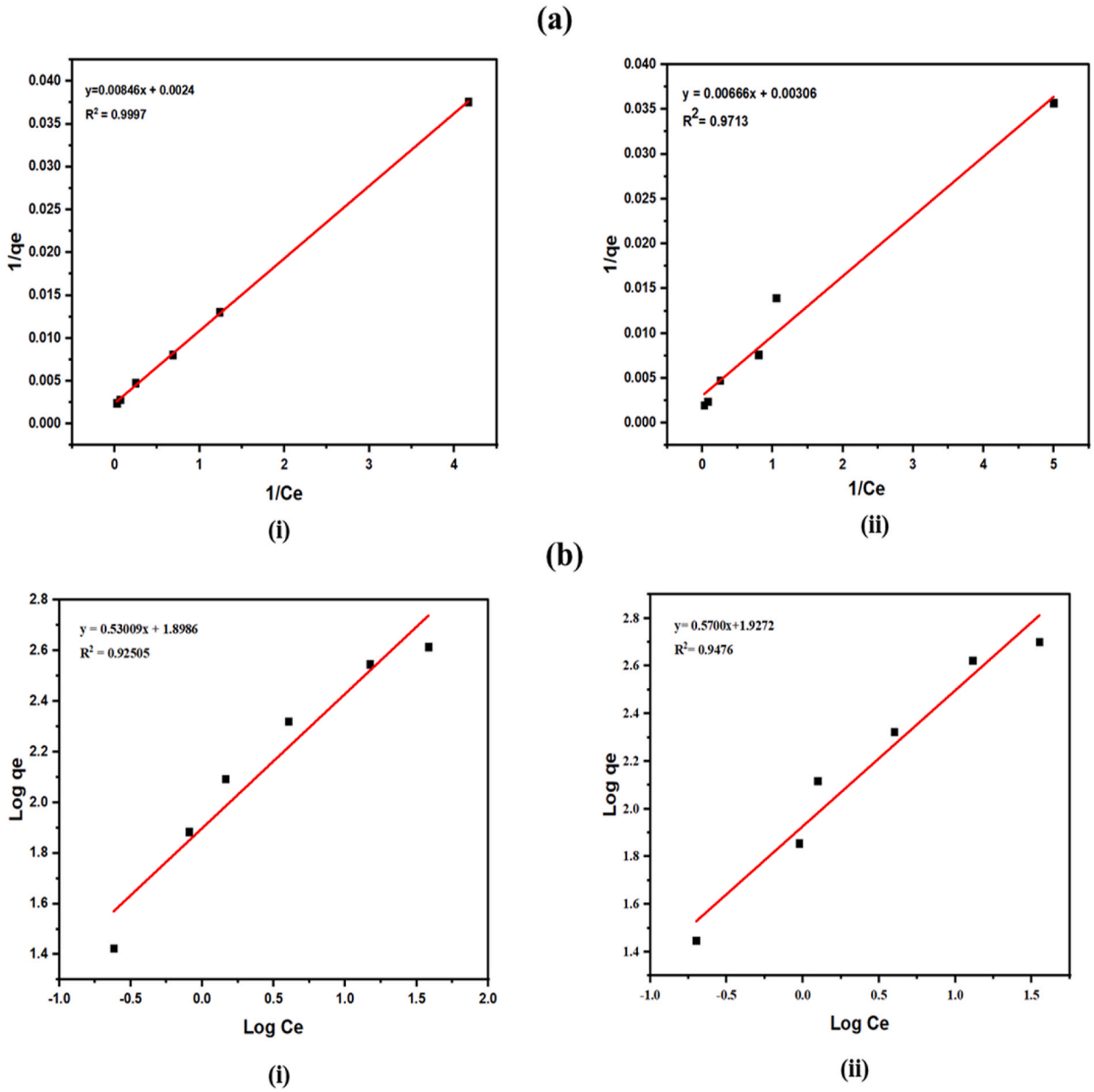

Fig. 5. (a) Langmuir isotherm plots for adsorption of; Lead (i) and Chromium (ii), (b) Freundlich isotherm plots for adsorption of; Lead (i) and Chromium (ii).

Table 6
Parameters of isotherm adsorption models for the adsorption of lead metal ions on iron oxide nanoparticles.

Type of isotherm	Parameter	Pb(II)	Cr(VI)
Langmuir	q_{max} (mg/g)	417	326.797
	K_L (L/mg	0.2840	0.4595
	R_L	0.4130	0.3033
	R^2	0.9997	0.9173
Freundlich	K_f	79.1771	84.5668
	1/n	0.5301	0.5700
	R^2	0.9251	0.9476

the slope and intercept of graph log q_e vs. log Ce as shown in Fig. 5(b). The parameters for the Freundlich model are written down in Table 6. Comparing the results of regression coefficient values for lead and chromium, we can find the best R^2 values for lead equal to 0.9251 and on the other hand, the best R^2 values of chromium are found to be 0.9476 for adsorption on IONPs. This indicates that adsorbates are adsorbed onto the heterogeneous surface of an adsorbent.

From Table 6, the Langmuir constant K_L value indicates the extent of interaction between the adsorbate and the surface. If the value of K_L is relatively larger it indicates that there is a strong interaction between adsorbate and adsorbent while a smaller value implies a weak interaction. Similarly, the values of R_L show how favorable the adsorption process is. $R_L = 0$ occurs if K_L is very large, meaning that adsorption is too strong and the reaction is irreversible. $0 < R_L < 1$ is the standard case when adsorption occurs normally under the set conditions. This means favorable adsorption. $R_L > 1$ implies unfavorable adsorption. If the denominator of the equation is negative, then R_L is negative and this is unfavorable adsorption.

The Freundlich constant K_f value also indicates Freundlich adsorption capacity. The parameter 1/n is a measure of deviation from linearity of adsorption between 0 and 1. For $1/n = 1$, the adsorption is linear. $1/n < 1$ implies physisorption while $1/n > 1$ indicates chemisorption. The more heterogeneous the surface, the closer the 1/n value is to 0. The values of K_f and 1/n from Table 6 indicate that the Freundlich isotherm fits the data better than the Langmuir isotherm. According to Semwal et al. [54], this suggests that the adsorption is heterogeneous rather than homogeneous. The surfaces of iron oxide nanoparticles are heterogenous as observed from the SEM analysis. These have different types of active sites with varying affinities for heavy metal ions therefore the Freundlich model accommodates this heterogeneity by considering multiple layers of adsorption on surfaces with different energies. Heterogeneous adsorption results in higher adsorption capacities because multiple layers of adsorption can occur on sites with different affinities. This is advantageous for applications where a high adsorption capacity is desirable. These findings are in agreement with the works of Stoian et al. [55]. The comparison of the developed nanoparticles with other iron oxide based adsorbents derived from steel wastes towards removal of the same heavy metal ions is shown in Table 7. The results show that the developed IONPs have better adsorption capacity, probably due to their high surface area developed from the synthesis process used.

3.3.3.3. Pseudo-first-order kinetics (Langergren's). Pseudo-first-order kinetic model was applied to study the rate of adsorption of lead and chromium ions on IONPs at equilibrium. Pseudo-first-order kinetics undergoes a physisorption process [59]. The plot of log(qe-qt) versus time (t) gives a straight line. K_1 and q_e are determined from the slope and intercept. The plots for pseudo-first-order are shown in Fig. 6(a). Values of K_1 and regression coefficient are shown in Table 8 for lead and chromium adsorption by IONPs. Comparing the values of the regression coefficient, the best values of R^2 at higher adsorbent doses (0.35 g) of IONPs is 0.9814 for lead adsorption. Whereas for chromium metal adsorption, the R^2 value was found to be 0.9907 when adsorbed to 0.35 g of IONPs. These values indicate that at such a concentration of adsorbent, the process of kinetic adsorption favors physisorption phenomena.

3.3.3.4. Pseudo-second-order kinetics. Pseudo-second-order kinetics follows the chemisorption process. The value of K_2 depends on experimental conditions such as initial concentration. Pseudo-second-order plots t/qt versus time (min) gave a straight line as indicated in Fig. 6(b). The values of k_2, qe, and R^2 are calculated from the plots and represented in Table 7. The linear correlation coefficient values R^2 are higher, at 0.9999 for IONPs dosage of 0.35 g for lead adsorption and 1 for IONPs dosage of 0.35 g chromium metal adsorption. The data suggests the chemisorption process, and it might be due to the exchange of metal ions with the functional groups of iron oxide NPs.

From Table 8, the values R^2 of the pseudo-first-order model are close to 1 which indicates that the adsorption is more inclined towards physisorption. The negative value of K_1 indicates that the data does not fit pseudo-first-order model. The adsorption fits well with the pseudo-second-order model, confirming chemisorption that involves valence forces through sharing or exchanging of electrons. According to Gupta et al. [60], the low value of rate constant (K_2) suggested that the adsorption rate decreased with the increase in time and the adsorption rate was proportional to the number of unoccupied sites. The relatively high surface area (325 m2/g) and

Table 7
Adsorption capacity of the developed iron oxide nanoparticles towards Pb (II) and Cr(VI) ions in comparison with other steel based adsorbents.

Source of steel waste	Iron oxide nanoparticle derived	Specific surface area (m^2/g)	Target heavy metal ion	Adsorption capacity (mg/g)	Reference
Iron oxide waste powder	Fe_3O_4	325.02	Pb (II)	417	This study
Mill scale	α-Fe_2O_3 modified with sodium alganite	5.43	Pb (II)	564	[23]
Steel Pickling Liqour	Fe_3O_4 modified with carboxymethyl-β-cyclodextrin polymer	–	Pb (II)	64.2	[56]
Steel Pickling Liqour	Fe_3O_4	–	Pb (II)	120.48	[26]
Iron oxide waste powder	Fe_3O_4	325.02	Cr (VI)	326.8	This study
Steel Pickling Liqour	Fe_3O_4 modified with sugarcane bagasse biochar	16.18	Cr (VI)	71.02	[57]
Steel Pickling Liqour	A mixture of α-Fe_2O_3 and Fe_3O_4 modified with sugarcane bagasse	29.92	Cr (VI)	24.48	[58]
Steel Pickling Liqour	Fe_3O_4 functionalized with ethylenediamine	28	Cr (VI)	81.5	[25]

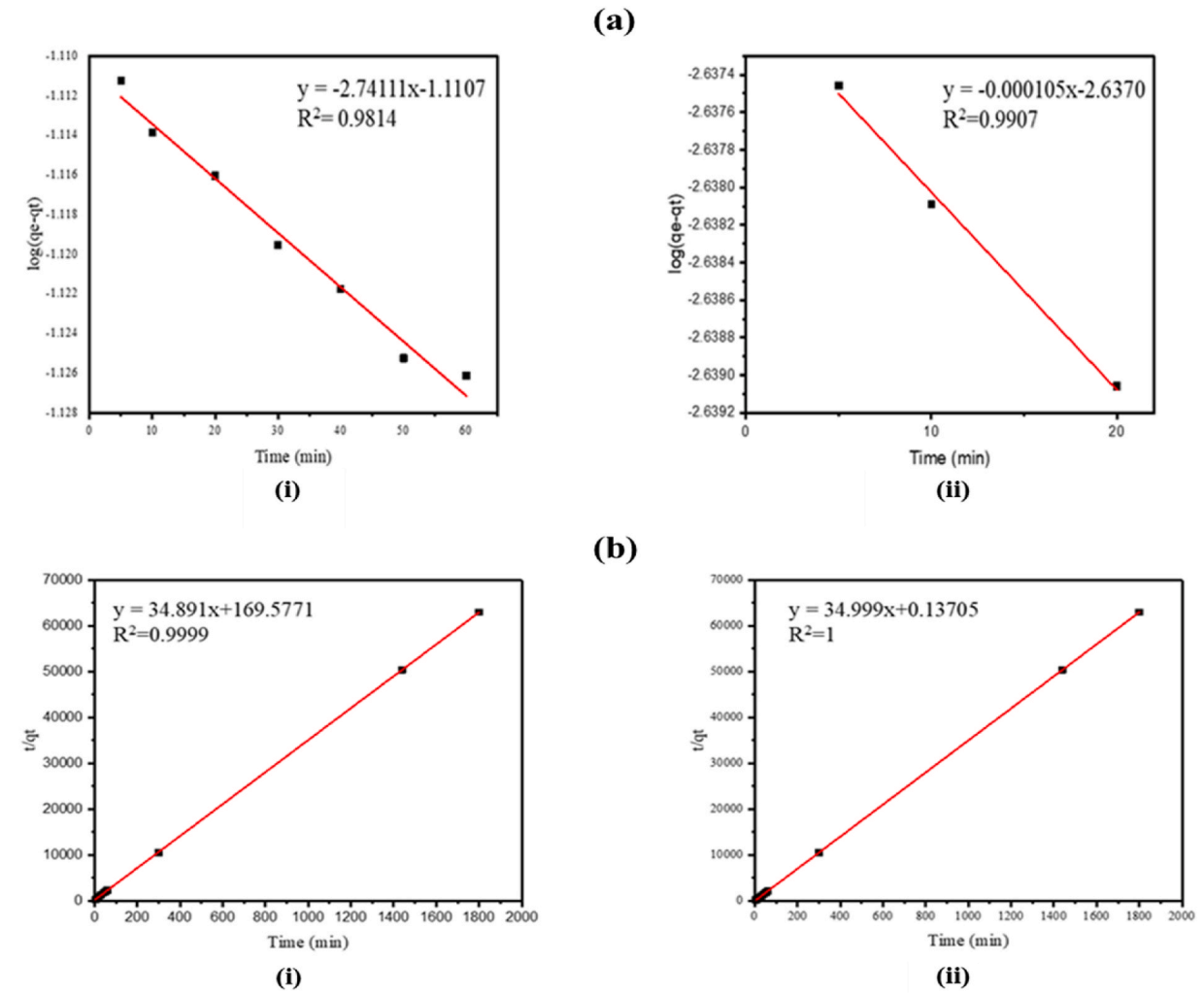

Fig. 6. (a) Pseudo 1st plots for adsorption of; Lead (i) and Chromium (ii), (b) Pseudo 2nd order plots for adsorption of; Lead (i) and Chromium (ii).

Table 8
Parameters of isotherm adsorption kinetics for adsorption of lead metal ions on iron oxide nanoparticles.

Pseudo-order kinetics	Parameter	Pb (II)	Cr (VI)
Pseudo-first-order parameters	K_1	−0.0457	−0.000005
	q_e	0.3293	0.0716
	R^2	0.9814	0.9907
Pseudo-second-order parameters	K_2	0.000872	10.8210
	q_e	0.0287	0.0286
	R^2	0.9999	1

porous nature of the developed nanoparticles could also support the chemisorption nature of adsorption [61]. The developed iron oxide nanoparticles had a higher affinity towards Pb (II) than Cr (VI) as indicated by the adsorption capacities. This mechanism was most likely due to ion exchange since an increase in contact time resulted into increased removal efficiency [56]. Furthermore, the adsorption of Cr (VI) can be attributed to its reduction by the developed Fe3O4 nanoparticles to Cr(III), which is then adsorbed through electrostatic interaction [62].

3.4. Evaluation of the effectiveness of iron oxide nanoparticles in Pb and Cr removal in an industrial effluent sample

To evaluate the effectiveness of the iron oxide nanoparticles, the industrial effluent sample that was collected from Global Paints Factory had concentrations of Pb and Cr as shown in Table 9. The measured concentrations of Pb (II) and Cr (VI) were above the

maximum permissible limits proposed by US EPA regulatory limit and national effluent discharge standards presented in Table 5. Heavy metals such as lead and chromium belong to the group of inorganic compounds and having a higher concentration than permissible limits can pollute water. These inorganic pollutants have a disruptive effect on public health and also on aquatic flora and fauna [63]. The results of the heavy metal removal percentages by the adsorption using iron oxide nanoparticles are shown in Table 8, indicating complete heavy metal removal at an adsorbent dosage of 0.35 g in 10 mL of industrial wastewater. This implies that per 30 mL of industrial wastewater, the optimal dose of the iron oxide nanoparticles is 1.05 g. From Equation (1), the removal percentage efficiency was found to be 100%. Other parameters that included turbidity, total alkalinity, total organic carbon, pH, apparent color and electrical conductivity were within the permissible limits as per the standards and the results are shown in Table 9. This is attributed to the particles' mesopore structure, high porosity, and large surface area which offer active sites for heavy metal adsorption from the effluent.

4. Conclusion

XRF analysis revealed that $Fe_2O_3$is the major compound contributing 97.23% of the total mass of the pickling red oxide waste. The oxide powders were not of nanoscale as most of the particles (27.3%) were retained on 250 μm sieve. The red oxide was haematitic as observed by the characteristic hematite FTIR peak at 540 cm^{-1}. BET analysis revealed a specific surface area of 9.72 m^2/g, suggesting a small amount of exposed surface area per gram of red oxide to favor adsorption processes. Iron oxide nanoparticles prepared using the wet chemical synthesis method with ammonia hydroxide solution as reducing agent were porous. The particles exhibited a heterogeneous structure with numerous pores of various sizes and shapes. FTIR analysis revealed the presence of active functional groups of hydroxyl bonds on the surface. Nanoparticles synthesized with 2.5% w/v of ammonia hydroxide solution had a surface area of 325.02 m^2/g. The particles were crystalline with a cubic structure, which is consistent with the crystal structure of magnetite (Fe_3O_4) and maghemite (γ-Fe_3O_4) phases. The synthesized iron oxide nanoparticles had an average size range of 20–30 nm. These characteristics favor adsorption processes.

Removal efficiencies for both lead and chromium contaminants at a concentration of 1 ppm were 100% at a dosage of 0.35 g of the nanoparticle in synthetic wastewater. The Freundlich isotherm model fitted adsorption data better, compared to Langmuir model, suggesting that adsorption occurred at heterogeneous sites on the surface of the iron oxide nanoparticles. R^2 values for Pb (II) and Cr (VI) showed the data best fitted to the pseudo-second-order model confirming chemisorption, which involves valence forces through sharing or exchanging of electrons. Results from the treatment of an effluent sample from a paint manufacturing plant showed that the nanoparticles successfully removed heavy metal pollutants of lead and chromium with an efficiency of 100%. Iron oxide nanoparticles developed from iron oxide pickling waste can thus be used to effectively remove lead and chromium pollutants from wastewater. This application provides an alternative use for steel pickling waste thus contributing to the circular economy in steel processing. The practical challenge with scaling up the technology lie in developing an optimum synthesis route to produce sufficient quantities of IONPs for industrial applications.

Funding information

This research was made possible with financial support from the Science, Technology and Innovation Secretariat, Office of the President of Uganda and Volkswagen Foundation, Grant 96659. The support of Roofings Rolling Mills, through their contact person, Mr. James Kasule is acknowledged. Sincere appreciation to Global Paints Factory for generously providing water samples used in this study.

Data availability statement

Data will be made available on request.

CRediT authorship contribution statement

Tumutungire Mwebembezi: Writing – review & editing, Writing – original draft, Methodology, Conceptualization. **Joel Wakatuntu:** Writing – review & editing, Project administration, Methodology, Data curation. **Joseph Jjagwe:** Writing – review & editing, Validation, Methodology, Investigation. **Christopher Kanyesigye:** Writing – review & editing, Validation, Methodology. **Robinah N. Kulabako:** Writing – review & editing, Supervision, Methodology, Funding acquisition, Formal analysis, Data curation. **Peter Wilberforce Olupot:** Writing – review & editing, Visualization, Validation, Supervision, Project administration, Methodology, Investigation, Funding acquisition, Data curation, Conceptualization.

Declaration of competing interest

The authors declare that they have no known competing financial interests or personal relationships that could have appeared to influence the work reported in this paper.

Table 9
Heavy metal and other parameters removal percentage with the application of Iron oxide nanoparticles as an adsorbent.

Adsorbate Dosage (g)	Heavy metal contaminant	Initial Concentration (mg/L)	Final Concentration (mg/L)	Percentage Removal (%)
0.35	Pb(II)	0.32	<0.01	100
	Cr(VI)	0.64	<0.01	100
TOC (mg/L)		19.9	19.9	N/A
Turbidity (FAU)		14	14	N/A
pH		7.5	7.5	N/A
Total Alkalinity (mg/L)		145	130	N/A
Apparent Color (PtCo)		82	82	N/A
EC (μs/cm)		947	930	N/A

References

[1] H. Ali, E. Khan, I. Ilahi, Environmental chemistry and ecotoxicology of hazardous heavy metals: environmental persistence, toxicity, and bioaccumulation, J. Chem. (2019) 6730305, https://doi.org/10.1155/2019/6730305, 2019.
[2] S. Cao, X. Duan, X. Zhao, Y. Chen, B. Wang, C. Sun, B. Zheng, F. Wei, Health risks of children's cumulative and aggregative exposure to metals and metalloids in a typical urban environment in China, Chemosphere 147 (2016) 404–411.
[3] Who, Lead in Drinking Water: Background Document for Development of WHO Guidelines for Drinking-Water Quality, WHO/SDE/WS, 2016, pp. 1–27. WHO/FWC/WSH/16.53.
[4] I. Manisalidis, E. Stavropoulou, A. Stavropoulos, E. Bezirtzoglou, Environmental and health impacts of air pollution: a review, Front. Public Heal. 8 (2020) 14, https://doi.org/10.3389/fpubh.2020.00014.
[5] H. Hossini, B. Shafie, A.D. Niri, M. Nazari, A.J. Esfahlan, M. Ahmadpour, Z. Nazmara, M. Ahmadimanesh, P. Makhdoumi, N. Mirzaei, A comprehensive review on human health effects of chromium: insights on induced toxicity, Environ. Sci. Pollut. Res. 29 (2022) 70686–70705.
[6] R. Shrestha, S. Ban, S. Devkota, S. Sharma, R. Joshi, A.P. Tiwari, H.Y. Kim, M.K. Joshi, Technological trends in heavy metals removal from industrial wastewater: a review, J. Environ. Chem. Eng. 9 (2021) 105688.
[7] K.O. Iwuozor, Prospects and challenges of using coagulation-flocculation method in the treatment of effluents, Adv. J. Chem. A. 2 (2019) 105–127.
[8] A. Zehra, M. Meena, P. Swapnil, N.A. Raytekar, R.S. Upadhyay, Sustainable approaches to remove heavy metals from water, Microb. Biotechnol. Basic Res. Appl. (2020) 127–146.
[9] W.S. Chai, J.Y. Cheun, P.S. Kumar, M. Mubashir, Z. Majeed, F. Banat, S.-H. Ho, P.L. Show, A review on conventional and novel materials towards heavy metal adsorption in wastewater treatment application, J. Clean. Prod. 296 (2021) 126589.
[10] S. Rajendran, A.K. Priya, P.S. Kumar, T.K.A. Hoang, K. Sekar, K.Y. Chong, K.S. Khoo, H.S. Ng, P.L. Show, A critical and recent developments on adsorption technique for removal of heavy metals from wastewater-A review, Chemosphere (2022) 135146.
[11] M.S. Mauter, I. Zucker, F. Perreault, J.R. Werber, J.-H. Kim, M. Elimelech, The role of nanotechnology in tackling global water challenges, Nat. Sustain. 1 (2018) 166–175, https://doi.org/10.1038/s41893-018-0046-8.
[12] P.N. Dave, L. V Chopda, Application of iron oxide nanomaterials for the removal of heavy metals, J. Nanotechnol. 2014 (2014) 398569, https://doi.org/10.1155/2014/398569.
[13] M. Chang, Y. Shih, Synthesis and application of magnetic iron oxide nanoparticles on the removal of Reactive Black 5: reaction mechanism, temperature and pH effects, J. Environ. Manag. 224 (2018) 235–242, https://doi.org/10.1016/j.jenvman.2018.07.021.
[14] S. Mahanty, S. Chatterjee, S. Ghosh, P. Tudu, T. Gaine, M. Bakshi, S. Das, P. Das, S. Bhattacharyya, S. Bandyopadhyay, P. Chaudhuri, Synergistic approach towards the sustainable management of heavy metals in wastewater using mycosynthesized iron oxide nanoparticles: biofabrication, adsorptive dynamics and chemometric modeling study, J. Water Process Eng. 37 (2020) 101426, https://doi.org/10.1016/j.jwpe.2020.101426.
[15] S. Chatterjee, S. Mahanty, P. Das, P. Chaudhuri, S. Das, Biofabrication of iron oxide nanoparticles using manglicolous fungus Aspergillus Niger BSC-1 and removal of Cr (VI) from aqueous solution, Chem. Eng. J. 385 (2020) 123790.
[16] N. Ajinkya, X. Yu, P. Kaithal, H. Luo, P. Somani, S. Ramakrishna, Magnetic iron oxide nanoparticle (IONP) synthesis to applications: present and future, Materials 13 (2020) 4644.
[17] M. Bustamante-Torres, D. Romero-Fierro, J. Estrella-Nuñez, B. Arcentales-Vera, E. Chichande-Proaño, E. Bucio, Polymeric composite of magnetite iron oxide nanoparticles and their application in biomedicine: a review, Polymers 14 (2022) 752.
[18] J. Jjagwe, P.W. Olupot, S. Carrara, Iron oxide nanoparticles/nanocomposites derived from steel and iron wastes for water treatment: a review, J. Environ. Manag. 343 (2023) 118236, https://doi.org/10.1016/j.jenvman.2023.118236.
[19] P. Mafabi, Utilization of Ferric Oxide Generated in the Acid Regeneration Plant in Paint Making (A Case Study: Roofings Rolling Mills Ltd, Namanve, Kampala), Kyambogo University, 2021 (unpublished work).
[20] I. Shajahan, J. George, S. Sivasankaran, K. Nair, Value addition to unutilized iron oxide generated from spent acid in chloride route TiO2 manufacturing process, Int. Res. J. Eng. Technol. 2 (2015) 1493–1498.
[21] S. Phearom, M.K. Shahid, Y.-G. Choi, Optimization of arsenic adsorption by mill scale–derived magnetite particles using response surface methodology, J. Hazardous, Toxic, Radioact. Waste. 25 (2021) 04021022, https://doi.org/10.1061/(asce)hz.2153-5515.0000620.
[22] N.A.A. Nazri, R.S. Azis, M.S. Mustaffa, A.H. Shaari, I. Ismail, H.C. Man, N.M. Saiden, N.H. Abdullah, Magnetite nanoparticles (MNPs) used as cadmium metal removal from the aqueous solution from mill scales waste sources, Sains Malays. 49 (2020) 847–858, https://doi.org/10.17576/jsm-2020-4904-14.
[23] M.E. Mahmoud, M.M. Saleh, M.M. Zaki, G.M. Nabil, A sustainable nanocomposite for removal of heavy metals from water based on crosslinked sodium alginate with iron oxide waste material from steel industry, J. Environ. Chem. Eng. 8 (2020) 104015, https://doi.org/10.1016/j.jece.2020.104015.
[24] N. Van Tien, V.X. Minh, L.T. Lu, N.T. Dung, R. Elements, L. Ha, C. Giay, Synthesis of Magnetic Nanoparticles from FeCl 2 Solution and Spent Pickling Liquor in Aqueous Saturated Lime Solution, 2019.
[25] X.B. Fang, Z.Q. Fang, P.K.E. Tsang, W. Cheng, X.M. Yan, L.C. Zheng, Selective adsorption of Cr(VI) from aqueous solution by EDA-Fe 3 O 4 nanoparticles prepared from steel pickling waste liquor, Appl. Surf. Sci. 314 (2014) 655–662, https://doi.org/10.1016/j.apsusc.2014.06.191.
[26] S.T. El-Wakeel, E.K. Radwan, A.S. El-Kalliny, T.A. Gad-Allah, I.Y. El-Sherif, Structural, magnetic and adsorption characteristics of magnetite nanoparticles prepared from spent pickle liquor, Int. J. ChemTech Res. 9 (2016) 373–382.
[27] H. Zeng, L. Zhai, J. Zhang, D. Li, As(V) adsorption by a novel core-shell magnetic nanoparticles prepared with Iron-containing water treatment residuals, Sci. Total Environ. 753 (2021) 142002, https://doi.org/10.1016/j.scitotenv.2020.142002.
[28] M. Shahrashoub, S. Bakhtiari, The efficiency of activated carbon/magnetite nanoparticles composites in copper removal: industrial waste recovery, green synthesis, characterization, and adsorption-desorption studies, Microporous Mesoporous Mater. 311 (2021) 110692, https://doi.org/10.1016/j.micromeso.2020.110692.
[29] E. Matijević, P. Scheiner, Ferric hydrous oxide sols: III. Preparation of uniform particles by hydrolysis of Fe(III)-chloride, -nitrate, and -perchlorate solutions, J. Colloid Interface Sci. 63 (1978) 509–524, https://doi.org/10.1016/S0021-9797(78)80011-3.
[30] K.A. Al-Saad, M.A. Amr, D.T. Hadi, R.S. Arar, M.M. Al-Sulaiti, T.A. Abdulmalik, N.M. Alsahamary, J.C. Kwak, Iron oxide nanoparticles: applicability for heavy metal removal from contaminated water, Arab J. Nucl. Sci. Appl. 45 (2012) 335–346.

[31] B. Chaloupková, Veronika, Tatiana Ivanova, Havrland, Sieve analysis of biomass : accurate method for determination of particle size distribution, Water Resour, Rural Dev (2016) 1012–1017.

[32] J. Dai, X. Yang, M. Hamon, L. Kong, Particle size controlled synthesis of CdS nanoparticles on a microfluidic chip, Chem. Eng. J. 280 (2015) 385–390, https://doi.org/10.1016/j.cej.2015.06.005.

[33] M.D. Shultz, W. Braxton, C. Taylor, E.E. Carpenter, One parameter control of the size of iron oxide nanoparticles synthesized in reverse micelles, J. Appl. Phys. 105 (2009) 07A522, https://doi.org/10.1063/1.3075983.

[34] E.E. Mensah, Z. Abbas, R.S. Azis, N.A. Ibrahim, A.M. Khamis, Complex permittivity and microwave absorption properties of OPEFB fiber-polycaprolactone composites filled with recycled hematite (α-Fe2O3) nanoparticles, Polymers 11 (2019) 1–11, https://doi.org/10.3390/polym11050918.

[35] M.R. Shenoy, S. Ayyasamy, M.V.R.V. Reddy, K. Govindan, T. Saravanakumar, T. Selvaraju, A.C. Jeyaramane, S. Adams, Preparation and characterization of porous iron oxide dendrites for photocatalytic application, Solid State Sci. 95 (2019) 105939, https://doi.org/10.1016/j.solidstatesciences.2019.105939.

[36] S. Sahoo, K. Agarwal, A. Singh, B. Polke, K. Raha, Characterization of γ- and α-Fe_2O_3 nano powders synthesized by emulsion precipitation-calcination route and rheological behaviour of α-Fe_2O_3, Int. J. Eng. Sci. Technol. 2 (2011) 118–126.

[37] D. Kostyukova, Y.H. Chung, Synthesis of iron oxide nanoparticles using isobutanol, J. Nanomater. 2016 (2016), https://doi.org/10.1155/2016/4982675.

[38] T.M. Laid, K. Abdelhamid, L.S. Eddine, B. Abderrhmane, Optimizing the biosynthesis parameters of iron oxide nanoparticles using central composite design, J. Mol. Struct. 1229 (2021) 129497, https://doi.org/10.1016/j.molstruc.2020.129497.

[39] Q. Yang, H. Kukino, H. Tatsuoka, The effects of gallium droplets on the morphologies and structures of -Fe2O3 nanostructures grown on iron substrates, J. Nanosci. Nanotechnol. 10 (2010) 7795–7799, https://doi.org/10.1166/jnn.2010.2890.

[40] N. Basavegowda, K. Mishra, Y.R. Lee, Sonochemically synthesized ferromagnetic Fe3O4 nanoparticles as a recyclable catalyst for the preparation of pyrrolo[3,4-c]quinoline-1,3-dione derivatives, RSC Adv. 4 (2014) 61660–61666, https://doi.org/10.1039/C4RA11623B.

[41] H. Maleki, A. Simchi, M. Imani, B.F.O. Costa, Size-controlled synthesis of superparamagnetic iron oxide nanoparticles and their surface coating by gold for biomedical applications, J. Magn. Magn Mater. 324 (2012) 3997–4005.

[42] M. Thommes, K. Kaneko, A. V Neimark, J.P. Olivier, F. Rodriguez-Reinoso, J. Rouquerol, K.S.W. Sing, Physisorption of gases, with special reference to the evaluation of surface area and pore size distribution (IUPAC Technical Report 87 (2015) 1051–1069.

[43] C. Zhang, Z. Yu, G. Zeng, B. Huang, H. Dong, J. Huang, Z. Yang, J. Wei, L. Hu, Q. Zhang, Phase transformation of crystalline iron oxides and their adsorption abilities for Pb and Cd, Chem. Eng. J. 284 (2016) 247–259.

[44] G. Delen, M. Monai, K. Stančiaková, B. Baumgartner, F. Meirer, B.M. Weckhuysen, Structure sensitivity in gas sorption and conversion on metal-organic frameworks, Nat. Commun. 14 (2023) 129.

[45] J. Pal, T. Pal, Faceted metal and metal oxide nanoparticles: design, fabrication and catalysis, Nanoscale 7 (2015) 14159–14190.

[46] M. Khanna, A. Mathur, A.K. Dubey, J. McLaughlin, I. Moirangthem, S. Wadhwa, D. Singh, R. Kumar, Rapid removal of lead(II) ions from water using iron oxide-tea waste nanocomposite - a kinetic study, IET Nanobiotechnol. 14 (2020) 275–280, https://doi.org/10.1049/iet-nbt.2019.0312.

[47] T.A. Aragaw, F.M. Bogale, B.A. Aragaw, Iron-based nanoparticles in wastewater treatment: a review on synthesis methods, applications, and removal mechanisms, J. Saudi Chem. Soc. 25 (2021) 101280, https://doi.org/10.1016/j.jscs.2021.101280.

[48] R. Abhinayaa, G. Jeevitha, D. Mangalaraj, N. Ponpandian, K. Vidhya, J. Angayarkanni, Cytotoxic consequences of Halloysite nanotube/iron oxide nanocomposite and iron oxide nanoparticles upon interaction with bacterial, non-cancerous and cancerous cells, Colloids Surfaces B Biointerfaces 169 (2018) 395–403.

[49] D. Morillo, M. Faccini, D. Amantia, G. Pérez, M.A. García, M. Valiente, L. Aubouy, Superparamagnetic iron oxide nanoparticle-loaded polyacrylonitrile nanofibers with enhanced arsenate removal performance, Environ. Sci.: Nano 3 (2016) 1165–1173, https://doi.org/10.1039/C6EN00167J.

[50] D. Epa, Office of water, office of science and technology, in: Chapter 3 Water Qual. Criteria. EPA-823-B-17-001, Environmental Protection Agency (EPA)., Washington, U.S, 2017, 2017, https://www.epa.gov/sites/production/files/2014-10/documents/handbook-chapter3.pdf.

[51] NEMA, National Environment, Standards for Discharge of Effluent into Water or Land) Regulations, 2020, p. CXIII.

[52] Y. Bagbi, A. Sarswat, D. Mohan, A. Pandey, P.R. Solanki, Lead and chromium adsorption from water using L-cysteine functionalized magnetite (Fe3O4) nanoparticles, Sci. Rep. 7 (2017) 7672, https://doi.org/10.1038/s41598-017-03380-x.

[53] R. Ezzati, Derivation of pseudo-first-order, pseudo-second-order and modified pseudo-first-order rate equations from Langmuir and Freundlich isotherms for adsorption, Chem. Eng. J. 392 (2020) 123705.

[54] N. Semwal, D. Mahar, M. Chatti, A. Dandapat, M. Chandra Arya, Adsorptive removal of Congo Red dye from its aqueous solution by Ag-Cu-CeO(2) nanocomposites: adsorption kinetics, isotherms, and thermodynamics, Heliyon 9 (2023) e22027, https://doi.org/10.1016/j.heliyon.2023.e22027.

[55] O. Stoian, C.I. Covaliu, G. Paraschiv, G.-A. Catrina (Traistaru, M. Niță-Lazăr, E. Matei, S. Ș Biriș, P. Tudor, Magnetite oxide nanomaterial used for lead ions removal from industrial wastewater, Materials 14 (2021), https://doi.org/10.3390/ma14112831.

[56] N.A.E. Emara, R.M. Amin, A.F. Youssef, S.A. Elfeky, Recycling of steel industry waste acid in the preparation of Fe3O4 nanocomposite for heavy metals remediation from wastewater, Rev. Chim. 71 (2021) 34–46, https://doi.org/10.37358/rc.20.12.8384.

[57] Y. Yi, G. Tu, D. Zhao, P.E. Tsang, Z. Fang, Key role of FeO in the reduction of Cr(VI) by magnetic biochar synthesised using steel pickling waste liquor and sugarcane bagasse, J. Clean. Prod. 245 (2020) 118886, https://doi.org/10.1016/j.jclepro.2019.118886.

[58] Y. Yi, G. Tu, D. Zhao, P.E. Tsang, Z. Fang, Biomass waste components significantly influence the removal of Cr(VI) using magnetic biochar derived from four types of feedstocks and steel pickling waste liquor, Chem. Eng. J. 360 (2019) 212–220, https://doi.org/10.1016/j.cej.2018.11.205.

[59] R. Gusain, N. Kumar, E. Fosso-Kankeu, S.S. Ray, Efficient removal of Pb(II) and Cd(II) from industrial mine water by a hierarchical MoS2/SH-mwcnt nanocomposite, ACS Omega 4 (2019) 13922–13935, https://doi.org/10.1021/acsomega.9b01603.

[60] V.K. Gupta, A. Rastogi, A. Nayak, Biosorption of nickel onto treated alga (Oedogonium hatei): application of isotherm and kinetic models, J. Colloid Interface Sci. 342 (2010) 533–539, https://doi.org/10.1016/j.jcis.2009.10.074.

[61] R. Fu, Y. Liu, Z. Lou, Z. Wang, S.A. Baig, X. Xu, Adsorptive removal of Pb(II) by magnetic activated carbon incorporated with amino groups from aqueous solutions, J. Taiwan Inst. Chem. Eng. 62 (2016) 247–258, https://doi.org/10.1016/j.jtice.2016.02.012.

[62] J. Niu, P. Ding, X. Jia, G. Hu, Z. Li, Study of the properties and mechanism of deep reduction and efficient adsorption of Cr(VI) by low-cost Fe3O4-modified ceramsite, Sci. Total Environ. 688 (2019) 994–1004, https://doi.org/10.1016/j.scitotenv.2019.06.333.

[63] K.L. Wasewar, S. Singh, S.K. Kansal, in: P. Devi, P. Singh (Eds.), Chapter 13 - Process Intensification of Treatment of Inorganic Water Pollutants, Elsevier, 2020, pp. 245–271. S.K.B.T.-I.P. in W. Kansal.